JℱM PAPERS

Small-amplitude heave oscillations of an annular disk

Muhammad Usman[1] and Hassan Masoud[1] (ID)

[1]Department of Mechanical Engineering, Clemson University, Clemson, SC 29634, USA
Corresponding author: Hassan Masoud, hmasoud@clemson.edu

We theoretically investigate the small-amplitude broadside oscillations of an annular disk within an unbounded fluid domain. Specifically, we formulate a semi-analytical framework to examine the effects of the oscillation frequency and pore radius on the disk's added mass and damping coefficients. By leveraging the superposition principle, we decompose the complex original problem into two simpler ones. The force exerted on the disk by the fluid is linked to the solutions of these sub-problems through the reciprocal theorem; the first solution is readily available, while the second is derived asymptotically, assuming a small inner radius. Both solutions are evaluated by transforming dual integral equations into systems of algebraic equations, which are then solved numerically. Building on these solutions, we extract asymptotic expressions for the variations of the quantities of interest in the limits of low and high oscillatory Reynolds numbers. Notably, at high frequencies, we uncover a previously overlooked logarithmic term in the force coefficient expansions, absent in prior scaling analyses of oscillating solid (impermeable) disks. Our findings indicate that, when viscosity plays a dominant role, an annular (porous) disk behaves similarly to a solid one, with reductions in the force coefficients scaling with the cube of the pore radius. We also discover, perhaps surprisingly, that, as inertial effects intensify, the damping coefficient initially increases with the pore radius, reaches a maximum and subsequently declines as the disk's inner hole enlarges further; at its peak, it can exceed the value for an equivalent solid disk by up to approximately 62 % in the asymptotic limit of extremely high oscillatory Reynolds number. Conversely, the added mass coefficient decreases monotonically with increasing porosity. The decay rate of the added mass in the inertial regime initially scales with the cube of the pore radius before transitioning to linear scaling when the pore radius is no longer extremely small. Although our analysis assumes a small pore radius, direct numerical simulations confirm that our asymptotic formulation remains accurate for inner-to-outer radius ratios up to at least $1/2$.

Key words: porous media, flow-structure interactions, mathematical foundations

1. Introduction

Heave plates are integral components in offshore engineering, particularly for enhancing the stability of structures such as platforms, buoys and floating wind turbines that are exposed to the dynamic forces of ocean waves (Ezoji, Shabakhty & Tao 2022). These broad, flat plates are installed at the base of floating structures to act as hydrodynamic dampers, effectively increasing the added mass and damping properties of the system. This increase often leads to reduced vertical motion, or heave, thereby enhancing the operational stability and safety of these structures. The practical implications of this enhanced stability are substantial, offering improved durability and reliability of offshore operations in challenging marine environments. Furthermore, in the field of renewable energy, heave plates are especially critical in the design of two-body point absorber wave energy converters, where they not only stabilise the device against the unpredictable nature of ocean waves but also influence the energy conversion efficiency by modulating the hydrodynamic interaction between wave forces and the converter itself (Brown & Thomson 2015; Tamakuwala *et al.* 2025). While the importance of heave plates is well recognised, the majority of the hydrodynamic research to date has concentrated on impermeable heave plates (see, e.g. He 2003). Therefore, the dynamics of porous heave plates, which could offer additional benefits (Downie *et al.* 2000*b*), remains underexplored. Porous plates have the potential to modify fluid flow patterns around the structure to enhance its performance under specific conditions. The interaction between water flow through the pores and the plate adds a layer of complexity absent in impermeable designs, potentially leading to more desired dynamic behaviour.

Among the limited studies that have examined the hydrodynamics of oscillating porous plates, the majority are experimental (Downie *et al.* 2000*a*; Vu, Chenu & Thiagarajan 2004; Chua *et al.* 2005; Molin, Remy & Rippol 2007; Tao & Dray 2008; Wadhwa, Thiagarajan & Pistani 2009; Wadhwa 2011; An & Faltinsen 2013; Li *et al.* 2013; Mentzoni & Kristiansen 2020; Ezoji *et al.* 2022), focusing on how amplitude variations affect the force coefficients during heave oscillations. Additionally, a few theoretical investigations utilised potential flow theory, integrated with a quadratic discharge law that governs the pressure drop through the pores, to estimate the force coefficients of perforated oscillating plates (Molin 1993, 2001; Molin *et al.* 2007; Liu *et al.* 2011; Molin 2011; An & Faltinsen 2013). Complementing these, several recent computational studies have simulated the flow around and through perforated plates undergoing heave oscillations (Nokob & Yeung 2018; Mentzoni & Kristiansen 2019*a*,*b*, 2020). The aforementioned studies generally find that porous plates provide additional damping at small amplitudes, attributing this effect to flow separation and vortex shedding. However, contrasting these findings, we reported increased damping in our previous theoretical investigation for porous objects, even in the absence of such phenomena (Jafari Kang *et al.* 2019), see also Sherwood (2020). In that study, we analysed the vibrations of porous cylinders at very small amplitudes, employing the Brinkman–Debye–Bueche model for permeable objects. This model accounts for the collective effect of pores through permeability (an indirect measure of porosity) rather than resolving individual pore flows. Notably, we discovered that the additional damping results from an increased phase shift between force and displacement.

The lack of a consensus on the mechanisms responsible for the change in the hydrodynamics of heave plates due to perforation underscores the need for further theoretical studies to elucidate the precise effects of perforation across a wide range of frequencies and amplitudes. To address this issue, here, we theoretically examine the elementary problem of an annular disk oscillating with a small amplitude in an unbounded fluid domain. We select this geometry because it represents the simplest form of a perforated heave plate with clearly defined porosity, thereby eliminating the need for
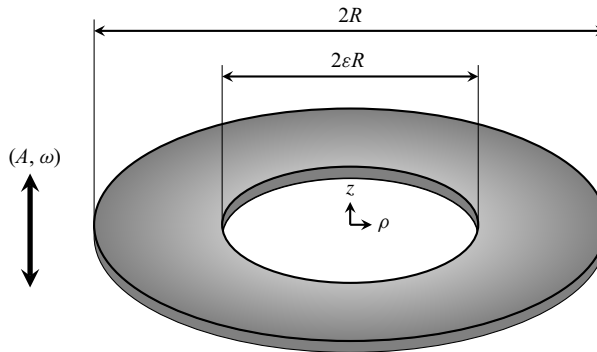
Figure 1. Schematics of an annular disk with outer radius R and inner-to-outer radius ratio of ε undergoing heave oscillations with amplitude A at frequency ω in the z direction within an unbounded fluid domain.

permeability-based continuum modelling to describe the flow through the disk. We employ a combination of the superposition principle, the reciprocal theorem and perturbation expansion to develop semi-analytical formulas for the variations in the added mass and damping coefficients of the annular disk as functions of oscillation frequency and pore radius. These formulations are further simplified in the asymptotic limits of low and high frequencies. Our solution strategy entails breaking down the problem into two more manageable sub-problems: one involving a solid disk vibrating in heave motion, and the other involving pressure-driven flow through a hole in an infinite plate. We apply Tranter's method to solve the dual integral equations that arise in each sub-problem. Our findings indicate that annular disks indeed provide additional damping (in excess of 60 % in extreme limits) as compared with their solid counterparts over specific ranges of oscillation frequency and pore radius. Additionally, we observe a reduction in the disk's added mass coefficient when it is made porous, independent of the oscillation frequency. Crucially, the small-amplitude assumption ensures that our predicted variations of the added mass and damping coefficients with pore radius and frequency are not caused by flow separation and vortex shedding, but instead result from changes in the phase relation between force and displacement, as discussed in § 3. For validation, we also solve the governing equations using a second-order finite-element method and demonstrate that our theoretical formulations retain their accuracy across a broad spectrum of parameters.

In what follows, we first describe the problem statement and our solution (§ 2). The results of our calculations are presented and discussed next (§ 3), followed by a short summary and concluding remarks (§ 4).

2. Problem formulation and solution

Consider an annular disk of outer radius R and inner-to-outer radius ratio of ε, oscillating sinusoidally with amplitude A at frequency ω within an unbounded, incompressible, Newtonian fluid of density ϱ and viscosity μ (see figure 1). Let (ρ, θ, z) represent a cylindrical coordinate system positioned at the centre of the disk, with the unit vector $\boldsymbol{e}_z$ normal to the broad side of the disk pointing upward, as shown in figure 1.

Suppose the disk's thickness is negligibly small and the amplitude of oscillations is much smaller than the outer radius of the disk ($A \ll R$), such that the convective inertia term in the Navier–Stokes equations can be neglected relative to the unsteady inertia term. This assumption may impose a stricter upper limit on the oscillation amplitude at high frequencies, since the associated error is expected to grow with increasing ω (see, e.g. Aureli, Basaran & Porfiri 2012). Under these conditions, the dynamics of the fluid flow

through and around the disk is governed by the linearised Navier–Stokes equations, which are expressed in dimensionless form below, along with the associated boundary conditions

$$\eta^2 \frac{\partial \tilde{\boldsymbol{u}}}{\partial \tilde{t}} = \boldsymbol{\nabla} \cdot \tilde{\boldsymbol{\sigma}} = \nabla^2 \tilde{\boldsymbol{u}} - \boldsymbol{\nabla} \tilde{p} \quad \text{and} \quad \boldsymbol{\nabla} \cdot \tilde{\boldsymbol{u}} = 0, \tag{2.1}$$

with the conditions

$$\tilde{\boldsymbol{u}} = \cos \tilde{t} \, \boldsymbol{e}_z \quad \text{for} \quad z = 0 \quad \text{and} \quad \varepsilon \leqslant \rho \leqslant 1,$$
$$\tilde{\boldsymbol{u}} \to \boldsymbol{0} \quad \text{as} \quad \sqrt{\rho^2 + z^2} \to \infty,$$
$$\tilde{p} = 0 \quad \text{for} \quad z = 0 \quad \text{when} \quad 0 \leqslant \rho < \varepsilon \quad \text{or} \quad \rho > 1. \tag{2.2}$$

The symbols $\tilde{t}$, $\tilde{\boldsymbol{u}}$, $\tilde{p}$ and $\tilde{\boldsymbol{\sigma}}$ in the above equations denote the dimensionless time, velocity field, pressure field and stress tensor, respectively. Also, $\eta^2 = \varrho R^2 \omega / \mu$ is the oscillatory Reynolds number that measures the time scale of vorticity diffusion relative to the oscillation period. Here, and throughout the article, the length, time, velocity and stress are non-dimensionalised by R, $1/\omega$, $A\omega$ and $\mu A \omega / R$, respectively.

Considering the sinusoidal nature of the disk's oscillations, it is mathematically advantageous to express the velocity, pressure and stress as real parts of complex quantities, specifically $\tilde{\boldsymbol{u}} = \text{Re}[\boldsymbol{u} \exp(i\tilde{t})]$, $\tilde{p} = \text{Re}[p \exp(i\tilde{t})]$ and $\tilde{\boldsymbol{\sigma}} = \text{Re}[\boldsymbol{\sigma} \exp(i\tilde{t})]$, with $i^2 = -1$. This transformation simplifies (2.1) and (2.2) to

$$i\eta^2 \boldsymbol{u} = \boldsymbol{\nabla} \cdot \boldsymbol{\sigma} = \nabla^2 \boldsymbol{u} - \boldsymbol{\nabla} p \quad \text{and} \quad \boldsymbol{\nabla} \cdot \boldsymbol{u} = 0, \tag{2.3}$$

with the boundary conditions

$$\boldsymbol{u} = \boldsymbol{e}_z \quad \text{for} \quad z = 0 \quad \text{and} \quad \varepsilon \leqslant \rho \leqslant 1,$$
$$\boldsymbol{u} \to \boldsymbol{0} \quad \text{as} \quad \sqrt{\rho^2 + z^2} \to \infty,$$
$$p = 0 \quad \text{for} \quad z = 0 \quad \text{when} \quad 0 \leqslant \rho < \varepsilon \quad \text{or} \quad \rho > 1. \tag{2.4}$$

Given the boundary conditions of this boundary-value problem, it follows that the velocity field is symmetric and the pressure field is antisymmetric with respect to the $z = 0$ plane. This ensures that the normal traction force remains continuous across the disk's two faces due to the change in the surface normal direction above and below the disk. Therefore, it is sufficient to consider the problem only in the upper half-space ($z \geqslant 0$), and express the force exerted on the disk by the fluid in the frequency domain as

$$\boldsymbol{F} = 2 \int_{S_d} \boldsymbol{n} \cdot \boldsymbol{\sigma} \, \mathrm{d}S = -2 \int_{S_d} p \, \mathrm{d}S \, \boldsymbol{e}_z = F \, \boldsymbol{e}_z, \tag{2.5}$$

where $\boldsymbol{n}$ is the unit normal vector and S_d denotes the upper surface of the annular disk. The dimensionless added mass, a, and damping coefficients, b, of the disk are then derived from the following relationship:

$$b + i a = -\frac{F}{\eta^2}, \tag{2.6}$$

where the added mass and damping coefficients are non-dimensionalised by ϱR^3 and $\varrho R^3 \omega$, respectively.

A solution strategy for solving the problem at hand and calculating a and b is to apply Hankel transforms to convert (2.3) and (2.4) to triple integral equations involving an unknown function which may be determined using the procedure outlined by Sneddon (1966). Here, however, we adopt an alternative approach that involves splitting

the original problem into two sub-problems, labelled with subscripts 0 and 1

$$\boldsymbol{u} = \boldsymbol{u}_0 + \boldsymbol{u}_1, \tag{2.7}$$

$$p = p_0 + p_1, \tag{2.8}$$

where $(\boldsymbol{u}_0, p_0)$ and $(\boldsymbol{u}_1, p_1)$, respectively, satisfy

$$i\eta^2 \boldsymbol{u}_0 = \boldsymbol{\nabla} \cdot \boldsymbol{\sigma}_0 = \nabla^2 \boldsymbol{u}_0 - \boldsymbol{\nabla} p_0 \quad \text{and} \quad \boldsymbol{\nabla} \cdot \boldsymbol{u}_0 = 0, \tag{2.9}$$

with

$$\boldsymbol{u}_0 = \boldsymbol{e}_z \quad \text{for} \quad z = 0 \quad \text{and} \quad 0 \leqslant \rho \leqslant 1,$$

$$\boldsymbol{u}_0 \to \boldsymbol{0} \quad \text{as} \quad \sqrt{\rho^2 + z^2} \to \infty,$$

$$p_0 = 0 \quad \text{for} \quad z = 0 \quad \text{and} \quad \rho > 1, \tag{2.10}$$

and

$$i\eta^2 \boldsymbol{u}_1 = \boldsymbol{\nabla} \cdot \boldsymbol{\sigma}_1 = \nabla^2 \boldsymbol{u}_1 - \boldsymbol{\nabla} p_1 \quad \text{and} \quad \boldsymbol{\nabla} \cdot \boldsymbol{u}_1 = 0, \tag{2.11}$$

with

$$\boldsymbol{u}_1 = \boldsymbol{0} \quad \text{for} \quad z = 0 \quad \text{and} \quad \varepsilon \leqslant \rho \leqslant 1,$$

$$\boldsymbol{u}_1 \to \boldsymbol{0} \quad \text{as} \quad \sqrt{\rho^2 + z^2} \to \infty,$$

$$p_1 = -p_0 \quad \text{for} \quad z = 0 \quad \text{and} \quad 0 \leqslant \rho < \varepsilon,$$

$$p_1 = 0 \quad \text{for} \quad z = 0 \quad \text{and} \quad \rho > 1. \tag{2.12}$$

Below, we present a force decomposition that stems from the above superposition, followed by the solution of these sub-problems.

2.1. *Force decomposition via reciprocal theorem*

Applying the reciprocal theorem (Masoud & Stone 2019) to the velocity–stress pairs $(\boldsymbol{u}, \boldsymbol{\sigma})$ and $(\boldsymbol{u}_0, \boldsymbol{\sigma}_0)$ yields

$$\int_S \boldsymbol{n} \cdot \boldsymbol{\sigma} \cdot \boldsymbol{u}_0 \ \mathrm{d}S = \int_S \boldsymbol{n} \cdot \boldsymbol{\sigma}_0 \cdot \boldsymbol{u} \ \mathrm{d}S = \int_S \boldsymbol{n} \cdot \boldsymbol{\sigma}_0 \cdot (\boldsymbol{u}_0 + \boldsymbol{u}_1) \ \mathrm{d}S, \tag{2.13}$$

where S denotes the surfaces enclosing the upper half of the fluid domain. The integrals over the bounding surface at infinity vanish due to the decay rate of the velocity and stress fields. After implementing the boundary conditions, (2.13) simplifies to

$$\int_{S_d} \boldsymbol{n} \cdot \boldsymbol{\sigma} \ \mathrm{d}S \cdot \boldsymbol{e}_z = \int_{S_{d,0}} \boldsymbol{n} \cdot \boldsymbol{\sigma}_0 \ \mathrm{d}S \cdot \boldsymbol{e}_z - \int_{S_{d,1}} p_0 \, \boldsymbol{u}_1 \ \mathrm{d}S \cdot \boldsymbol{e}_z, \tag{2.14}$$

where $S_{d,0}$ and $S_{d,1}$ represent areas of $z = 0$ plane confined to $0 \leqslant \rho \leqslant 1$ and $0 \leqslant \rho < \varepsilon$, respectively. Let us define

$$F_0 = 2 \int_{S_{d,0}} \boldsymbol{n} \cdot \boldsymbol{\sigma}_0 \ \mathrm{d}S \cdot \boldsymbol{e}_z = -2 \int_{S_{d,0}} p_0 \ \mathrm{d}S, \tag{2.15}$$

$$F_1 = -2 \int_{S_{d,1}} p_0 \, (\boldsymbol{u}_1 \cdot \boldsymbol{e}_z) \ \mathrm{d}S. \tag{2.16}$$

Referring back to (2.5), the total fluid force on the disk can now be expressed as the sum of contributions from the two sub-problems as

$$F = F_0 + F_1. \tag{2.17}$$

Consequently, the added mass and damping coefficients can be decomposed as

$$a = a_0 + a_1, \tag{2.18}$$

$$b = b_0 + b_1. \tag{2.19}$$

Here, a_0 and b_0 represent the contributions from the primary sub-problem, while a_1 and b_1 account for the additional effects introduced by the secondary sub-problem.

2.2. *First sub-problem*

For completeness, we reiterate the solution steps here. By applying Hankel transforms to (2.9), solving the resulting equations using the boundary conditions specified in (2.10) and then performing inverse Hankel transforms, the following expressions can be derived for the velocity and pressure fields:

$$\boldsymbol{u}_0 \cdot \boldsymbol{e}_\rho = \int_0^\infty k A(k) \left(e^{-kz} - e^{-\xi z} \right) J_1(k\rho) \ \mathrm{d}k, \tag{2.20}$$

$$\boldsymbol{u}_0 \cdot \boldsymbol{e}_z = \int_0^\infty k A(k) \left(e^{-kz} - \frac{k}{\xi} e^{-\xi z} \right) J_0(k\rho) \ \mathrm{d}k, \tag{2.21}$$

$$p_0 = i\eta^2 \int_0^\infty A(k) \, e^{-kz} \, J_0(k\rho) \ \mathrm{d}k, \tag{2.22}$$

where $\xi^2 = k^2 + i\eta^2$, J is the Bessel function of the first kind, and the unknown function $A(k)$ satisfies

$$\int_0^\infty k A(k) \left(1 - \frac{k}{\xi} \right) J_0(kr) \ \mathrm{d}k = 1 \quad \text{for} \quad 0 \leqslant \rho \leqslant 1, \tag{2.23}$$

$$\int_0^\infty A(k) \, J_0(kr) \ \mathrm{d}k = 0 \quad \text{for} \quad \rho > 1. \tag{2.24}$$

Following Tranter's method (Tranter 1966), $A(k)$ can be assumed to take the form of

$$A(k) = \sqrt{\frac{2k}{\pi}} \sum_{m=0}^\infty \alpha_m J_{2m+1/2}(k) \quad \text{for} \quad m = 0, 1, 2 \cdots. \tag{2.25}$$

This representation reduces the above dual integral equations to a system of linear algebraic equations for α_m

$$\sum_{m=0}^\infty \alpha_m \int_0^\infty k \left(1 - \frac{k}{\xi} \right) J_{2m+1/2}(k) \, J_{2n+1/2}(k) \ \mathrm{d}k = \delta_{0n} \quad \text{for} \quad n = 0, 1, \cdots, \tag{2.26}$$

with δ_{ij} being the Kronecker delta function. Equation (2.26) can be solved numerically using standard approaches. Substituting $A(k)$ from (2.25) into (2.22) and performing surface integration of the subsequent equation leads to (after some simplifications) the following formulas for the pressure and force on the disk:

$$\hat{p}_0 = \frac{2i\eta^2}{\sqrt{\pi}} \sum_{m=0}^\infty \frac{\Gamma(m+1) \, \alpha_m}{\Gamma(m+1/2)} \, {}_2F_1(m+1, 1/2 - m; 1; \rho^2), \tag{2.27}$$

$$F_0 = -2 \int_{S_{d,0}} p_0 \ \mathrm{d}S = -8i\eta^2 \alpha_0, \tag{2.28}$$

where $_2F_1$ is the hypergeometric function and the hat symbol indicates evaluation at the surface of the disk.

2.3. *Second sub-problem*

This problem describes the fluid flow through and around a stationary annular disk driven by the pressure difference across the disk required to cancel out the contribution from the first sub-problem over the disk's orifice. Solving for $(\boldsymbol{u}_1, p_1)$ without constraints on the pore size of the disk is challenging. Hence, we aim to develop an asymptotic solution in the limit of small ε. As demonstrated in the forthcoming section (§ 3), the approximation error of our solution remains minimal even when ε is as large as $1/2$ and, in some cases, beyond.

We use a Taylor series expansion to approximate the pressure distribution on the disk from the prior sub-problem as

$$\hat{p}_0 = \hat{p}_0\big|_{\rho=0} + \frac{\mathrm{d}\hat{p}_0}{\mathrm{d}\rho}\bigg|_{\rho=0} \rho + \frac{1}{2}\frac{\mathrm{d}^2\hat{p}_0}{\mathrm{d}\rho^2}\bigg|_{\rho=0} \rho^2 + \cdots, \tag{2.29}$$

where

$$\hat{p}_0\big|_{\rho=0} = \frac{2i\eta^2}{\sqrt{\pi}} \sum_{m=0}^{\infty} \frac{\Gamma(m+1)}{\Gamma(m+1/2)} \alpha_m. \tag{2.30}$$

Substituting the above relation in (2.12) and then retaining only the first term in the expansion, we arrive at the following equations for $(\boldsymbol{u}_1^{(1)}, p_1^{(1)})$, which are the leading-order contributions to $(\boldsymbol{u}_1, p_1)$ when $\varepsilon \ll 1$:

$$i\eta^2 \boldsymbol{u}_1^{(1)} = \boldsymbol{\nabla} \cdot \boldsymbol{\sigma}_1^{(1)} = \nabla^2 \boldsymbol{u}_1^{(1)} - \boldsymbol{\nabla} p_1^{(1)} \quad \text{and} \quad \boldsymbol{\nabla} \cdot \boldsymbol{u}_1^{(1)} = 0, \tag{2.31}$$

with

$$\boldsymbol{u}_1^{(1)} = \boldsymbol{0} \quad \text{for} \quad z = 0 \quad \text{and} \quad \varepsilon \leqslant \rho \leqslant 1,$$
$$\boldsymbol{u}_1^{(1)} \to \boldsymbol{0} \quad \text{as} \quad \sqrt{\rho^2 + z^2} \to \infty,$$
$$p_1^{(1)} = -\hat{p}_0\big|_{\rho=0} \quad \text{for} \quad z = 0 \quad \text{and} \quad 0 \leqslant \rho < \varepsilon,$$
$$p_1^{(1)} = 0 \quad \text{for} \quad z = 0 \quad \text{and} \quad \rho > 1. \tag{2.32}$$

The problem posed by (2.31) and (2.32) essentially corresponds to the flow through a pore in an infinite plate, due to the pressure differential $2\hat{p}_0\big|_{r=0}$. This interpretation is substantiated by rescaling the lengths with ε.

Applying the same steps employed to solve the first sub-problem, we obtain

$$\boldsymbol{u}_1^{(1)} \cdot \boldsymbol{e}_\rho = \int_0^\infty k B(k)\big(e^{-kz} - e^{-\xi z}\big) J_1(k\rho) \ \mathrm{d}k, \tag{2.33}$$

$$\boldsymbol{u}_1^{(1)} \cdot \boldsymbol{e}_z = \int_0^\infty k B(k) \left(e^{-kz} - \frac{k}{\xi} e^{-\xi z}\right) J_0(k\rho) \ \mathrm{d}k, \tag{2.34}$$

$$p_1^{(1)} = i\eta^2 \int_0^\infty B(k) \, e^{-kz} \, J_0(k\rho) \ \mathrm{d}k, \tag{2.35}$$

where the unknown function $B(k)$ satisfies the dual integral equations

$$\int_0^\infty B(k) \, J_0(k\rho) \ \mathrm{d}k = ip^\star \quad \text{for} \quad 0 \leqslant \rho \leqslant \varepsilon, \tag{2.36}$$

$$\int_0^\infty k B(k) \left(1 - \frac{k}{\xi}\right) J_0(k\rho) \ \mathrm{d}k = 0 \quad \text{for} \quad \rho > \varepsilon, \tag{2.37}$$

where $p^{\star} = \hat{p}_0\big|_{\rho=0}/\eta^2$. Following Tranter's method (Tranter 1966) once again, we represent $B(k)$ as a series of Bessel functions

$$B(k) = ip^{\star} \sqrt{\frac{2k\varepsilon}{\pi}} \left[k \left(1 - \frac{k}{\xi} \right) \right]^{-1} \sum_{m=0}^{\infty} \beta_m \, J_{2m+1/2}(k\varepsilon). \tag{2.38}$$

This formulation inherently satisfies the velocity boundary condition on the disk. Upon substituting for $B(k)$ from (2.38) into (2.36), and then multiplying both sides by

$$\frac{\tilde{\rho}}{\sqrt{1 - \tilde{\rho}^2}} \, {}_2F_1(-n, n + 1/2; 1; \tilde{\rho}^2), \tag{2.39}$$

and integrating both sides with respect to $\tilde{\rho} = \rho/\varepsilon$ from 0 to 1 (see also Erdogan & Bahar 1964), we reach

$$\sum_{m=0}^{\infty} \beta_m \int_0^{\infty} \left[\tilde{k} \left(1 - \frac{\tilde{k}}{\tilde{\xi}} \right) \right]^{-1} J_{2m+1/2}(\tilde{k}) \, J_{2n+1/2}(\tilde{k}) \, \mathrm{d}\tilde{k} = \delta_{0n} \quad \text{for} \quad n = 0, 1, \cdots, \tag{2.40}$$

where $\tilde{k} = k\varepsilon$, $\tilde{\xi}^2 = \tilde{k}^2 + i\tilde{\eta}^2$ and $\tilde{\eta}^2 = \eta^2\varepsilon^2$. Equation (2.40) constitutes a system of linear algebraic questions for β_m that can be numerically solved in a manner similar to (2.26). Given (2.16), (2.34) and (2.38), it is straightforward to show that the leading-order contribution to F_1 is given by

$$\begin{aligned}
F_1^{(1)} &= -4\pi\eta^2 p^{\star} \int_0^{\varepsilon} \left(\boldsymbol{u}_1^{(0)}\big|_{z=0} \cdot \boldsymbol{e}_z \right) \rho \, \mathrm{d}\rho \\
&= 4i\eta^2 \sqrt{2\varepsilon\pi} \, p^{\star 2} \sum_{m=0}^{\infty} \beta_m \int_0^{\varepsilon} \rho \int_0^{\infty} \sqrt{k} \, J_{2m+1/2}(k\varepsilon) \, J_0(k\rho) \, \mathrm{d}k \, \mathrm{d}\rho \\
&= -8i\eta^2 p^{\star 2} \beta_0 \, \varepsilon.
\end{aligned} \tag{2.41}$$

2.4. *Limit of low oscillatory Reynolds number*

Williams (1966) elegantly demonstrated that the force exerted on an arbitrarily shaped body undergoing slow oscillations can be expressed asymptotically in the limit of small η as

$$F = F_s \left(1 - \frac{F_s}{6\pi} e^{i\pi/4} \, \eta \right) + \mathcal{O}(\eta^2), \tag{2.42}$$

where F_s represents the Stokes ($\eta = 0$) drag on the body. Below, we derive F_s for our annular disk, continuing to assume that $\varepsilon \ll 1$. By fixing $\eta = 0$, the equations for the pressure distribution and force on the solid disk in the first sub-problem, and the velocity distribution in the z direction and the force in the second problem, simplify to the following (refer to Happel & Brenner 1983; Davis 1991; Tanzosh & Stone 1996a, for more detail):

$$p_{0,s} = \frac{4}{\pi} \int_0^{\infty} \sin k \, e^{-kz} J_0(k\rho) \, \mathrm{d}k, \tag{2.43}$$

$$F_{0,s} = -4\pi \int_0^1 p_0 \, \rho \, \mathrm{d}\rho = -16, \tag{2.44}$$

$$\boldsymbol{u}_{1,s}^{(1)} \cdot \boldsymbol{e}_z = \frac{4}{\pi^2} \int_0^{\infty} \frac{\mathrm{d}}{\mathrm{d}k} \left[\frac{\sin(k\varepsilon)}{k} \right] (1 + kz) \, e^{-kz} J_0(kr) \, \mathrm{d}k, \tag{2.45}$$

$$F_{1,s}^{(1)} = -4\pi \left. \hat{p}_{0,s} \right|_{\rho=0} \int_0^\varepsilon \left(\left. \boldsymbol{u}_{1,s}^{(0)} \right|_{z=0} \cdot \boldsymbol{e}_z \right) \rho \ \mathrm{d}\rho = \frac{64\varepsilon^3}{3\pi^2}, \tag{2.46}$$

where $\left. \hat{p}_{0,s} \right|_{\rho=0} = 4/\pi$. In this setting, closed-form expressions for the pressure and velocity fields are also obtainable in oblate spheroidal coordinates (for additional details, see again Happel & Brenner 1983; Davis 1991; Tanzosh & Stone 1996*a*). Given (2.44) and (2.46), the Stokes drag on the annular disk in the limit of small pore radius can be written asymptotically as

$$F_s = -16 \left(1 - \frac{4\varepsilon^3}{3\pi^2} \right) + \cdots, \tag{2.47}$$

which is precisely what is arduously derived by Davis (1991*b*).

2.5. *Limit of high oscillatory Reynolds number*

When the oscillatory Reynolds number becomes very large ($\eta \to \infty$), we consider two sub-limits based on the magnitude of $\tilde{\eta} = \eta\varepsilon$ as discussed below.

2.5.1. *Sub-limit of $\tilde{\eta} \gg 1$*

In cases where both η and $\tilde{\eta}$ are much greater than one, it can be shown that the original problem, to the leading order, reduces to the following mixed boundary-value problem for the velocity potential ϕ:

$$\nabla^2 \phi = 0, \tag{2.48}$$

with

$$
\begin{aligned}
\boldsymbol{n} \cdot \boldsymbol{\nabla}\phi = 1 \quad &\text{for} \quad z = 0 \quad \text{and} \quad \varepsilon \leqslant \rho \leqslant 1, \\
\phi = 0 \quad &\text{for} \quad z = 0 \quad \text{when} \quad 0 \leqslant \rho < \varepsilon \quad \text{or} \quad \rho > 1, \\
\phi \to 0 \quad &\text{as} \quad \sqrt{\rho^2 + z^2} \to \infty,
\end{aligned}
\tag{2.49}
$$

where the velocity and pressure fields in this limit are calculated from $\boldsymbol{u}_\infty = \boldsymbol{\nabla}\phi$ and $p_\infty = -i\eta^2\phi$, respectively. The potential fields and forces associated with the sub-problems of the above problem are given by (see, e.g. Lamb 1945; Sneddon 1966; Gradshteyn & Ryzhik 2007)

$$\phi_0 = \frac{2}{\pi} \int_0^\infty \frac{d}{\mathrm{d}k} \left[\frac{\sin k}{k} \right] e^{-kz} J_0(kr) \ \mathrm{d}k, \tag{2.50}$$

$$F_{0,\infty} = 4\pi i \eta^2 \int_0^1 \phi_0 \, \rho \ \mathrm{d}\rho = -\frac{8}{3} i \eta^2, \tag{2.51}$$

$$\phi_1^{(1)} = -\frac{2}{\pi} \left. \hat{\phi}_0 \right|_{r=0} \int_0^\infty \frac{\sin(k\varepsilon)}{k} e^{-kz} J_0(kr) \ \mathrm{d}k, \tag{2.52}$$

$$F_{1,\infty}^{(1)} = 4\pi i \eta^2 \left. \phi_0 \right|_{r=0} \int_0^\varepsilon \boldsymbol{n} \cdot \boldsymbol{\nabla}\phi_1^{(0)} \, \rho \ \mathrm{d}\rho = \frac{32\varepsilon}{\pi^2} i \eta^2, \tag{2.53}$$

where

$$\left. \hat{\phi}_0 \right|_{r=0} = -2/\pi, \tag{2.54a}$$

$$\boldsymbol{u}_{0,\infty} = \boldsymbol{\nabla}\phi_0, \tag{2.54b}$$

Asymptotic limits

Coefficients	$\eta \to 0$	$\eta \to \infty$
$a_0 = 8\alpha_{0,r}$	$\dfrac{64\sqrt{2}}{3\pi\eta}$	$\dfrac{8}{3} + \dfrac{\mathcal{A}_a \ln\eta + \mathcal{B}_a}{\eta}$
$b_0 = -8\alpha_{0,i}$	$\dfrac{16}{\eta^2} + \dfrac{64\sqrt{2}}{3\pi\eta}$	$\dfrac{\mathcal{A}_b \ln\eta + \mathcal{B}_b}{\eta}$
$p_r^\star = \mathrm{Re}(p^\star)$	$\dfrac{4}{\pi\eta^2} + \dfrac{16\sqrt{2}}{3\pi^2\eta}$	$\dfrac{\mathcal{A}_r^p \ln\eta + \mathcal{B}_r^p}{\eta}$
$p_i^\star = \mathrm{Im}(p^\star)$	$\dfrac{16\sqrt{2}}{3\pi^2\eta}$	$\dfrac{2}{\pi} + \dfrac{\mathcal{A}_i^p \ln\eta + \mathcal{B}_i^p}{\eta}$
	$\tilde{\eta} \to 0$	$\tilde{\eta} \to \infty$
$\beta_{0,r} = \mathrm{Re}(\beta)$	$\mathcal{C}\tilde{\eta}^4$	$1 - \dfrac{\mathcal{A}_r^\beta \ln\tilde{\eta} + \mathcal{B}_r^\beta}{\tilde{\eta}}$
$\beta_{0,i} = \mathrm{Im}(\beta)$	$\dfrac{\tilde{\eta}^2}{6}$	$\dfrac{\mathcal{A}_i^\beta \ln\tilde{\eta} + \mathcal{B}_i^\beta}{\tilde{\eta}}$

Table 1. Asymptotic expressions describing the variations of a_0, b_0 and $p^\star$ as functions of η, along with the dependence of β_0 on $\tilde{\eta}$. The coefficients $\mathcal{A}$, $\mathcal{B}$ and $\mathcal{C}$ are numerically computed and their values are reported in table 2.

$$\boldsymbol{u}_{1,\infty}^{(1)} = \boldsymbol{\nabla}\phi_1^{(1)}, \tag{2.54c}$$

$$p_{0,\infty} = -i\eta^2\phi_0, \tag{2.54d}$$

$$p_{1,\infty}^{(1)} = -i\eta^2\phi_1^{(1)}. \tag{2.54e}$$

Hence, in the potential flow limit, the hydrodynamic force on an annular disk asymptotically takes the form

$$F_\infty = -\frac{8}{3}i\eta^2\left(1 - \frac{12\varepsilon}{\pi^2}\right) + \cdots. \tag{2.55}$$

It is worth noting that the velocity potentials in (2.50) and (2.52) can be alternatively expressed in closed form in oblate spheroidal coordinates (see, e.g. Lamb 1945).

2.5.2. *Sub-limit of $\tilde{\eta} \ll 1$*

In the regime in which $\varepsilon \ll 1/\eta$ while $\eta \gg 1$, the leading-order solution to the first problem remains the same as the one given by (2.50) and (2.51), i.e.

$$F_0 = F_{0,\infty} + \mathcal{O}(\eta \ln\eta). \tag{2.56}$$

The origin of the $\mathcal{O}(\eta \ln\eta)$ correction in the above equation will be discussed in § 3 (see also table 1).

Since $\tilde{\eta} \ll 1$, the solution to the second problem follows from (2.45) and (2.46) for Stokes flow through a circular hole in an infinite wall. Given that the driving pressure here
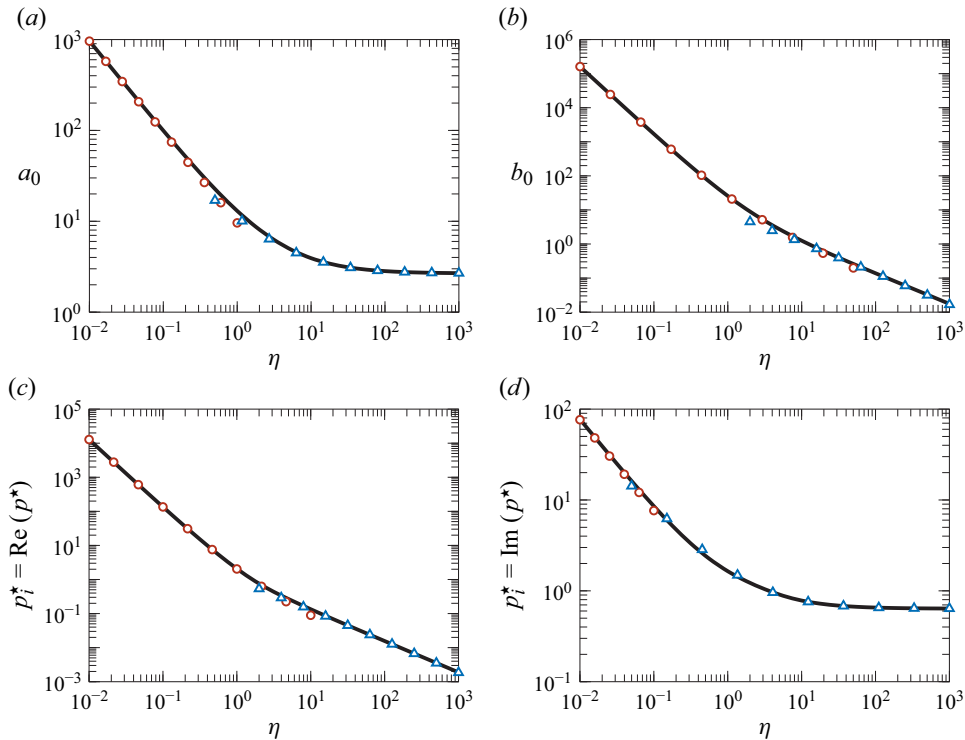
Figure 2. Plots of dimensionless (*a*) added mass and (*b*) viscous damping coefficients of a solid disk (denoted by a_0 and b_0, respectively), along with the (*c*) real and (*d*) imaginary components of the normalised pressure at the centre of the solid disk (defined as $p^\star = \hat{p}_0|_{\rho=0}/\eta^2$), all versus the square root of the oscillatory Reynolds number η. Red circular and blue triangular symbols correspond to the asymptotic formulas for the low- and high-frequency limits, respectively, as listed in table 1.

is $\hat{p}_{0,\infty}|_{\rho=0}$ rather than $\hat{p}_{0,s}|_{\rho=0}$, we then obtain

$$F_{1,\infty,s} = \left(\frac{\hat{p}_{0,\infty}\big|_{\rho=0}}{\hat{p}_{0,s}\big|_{\rho=0}} \right)^2 F_{1,s}^{(1)} + \mathcal{O}\!\left(\varepsilon^3 \eta^3 \ln \eta\right) = -\frac{16\varepsilon^3 \eta^4}{3\pi^2} + \mathcal{O}\!\left(\varepsilon^3 \eta^3 \ln \eta\right). \quad (2.57)$$

3. Results and discussion

3.1. *Baseline: a solid disk*

For the baseline case of a solid disk, we solve a linear system of equations based on (2.26) to obtain α_m for $m = 0, 1, \ldots, 10$ across a range of η from 10^{-2} to 10^3. Accordingly, we retain the first ten terms in the series and evaluate the improper integrals using a global adaptive quadrature with a strict absolute tolerance to maintain accuracy. Using the computed values of α_m, we employ (2.5), (2.28) and (2.30) to determine the added mass and damping coefficients, denoted by a_0 and b_0, respectively, and to compute the normalised pressure at the centre of the disk, defined as $p^\star = \hat{p}_0\big|_{\rho=0}/\eta^2$. For the pressure, repeated Shanks transformation is used to accelerate the convergence of the series.

The results of these calculations are presented as solid black lines in figure 2, where red circular and blue triangular symbols represent, respectively, the asymptotic expressions for a_0, b_0 and $p^\star$ in the limits of low and high frequencies, as outlined in table 1. A key observation is that the asymptotic curves closely overlap in an intermediate range

$\mathcal{A}_a$	$\mathcal{A}_b$	$\mathcal{A}_r^p$	$\mathcal{A}_i^p$	$\mathcal{A}_r^\beta$	$\mathcal{A}_i^\beta$	
1.700	1.235	0.126	0.144	0.227	0.237	
$\mathcal{B}_a$	$\mathcal{B}_b$	$\mathcal{B}_r^p$	$\mathcal{B}_i^p$	$\mathcal{B}_r^\beta$	$\mathcal{B}_i^\beta$	$\mathcal{C}$
8.349	8.155	0.984	1.112	1.186	0.780	0.050

Table 2. Numerically computed values of the coefficients appearing in table 1.

of η, demonstrating their combined accuracy across the entire frequency spectrum. The low-frequency asymptotic formulas result directly from the derivation presented in §2.4. These expressions are found to be in full agreement with the results reported by Zhang & Stone (1998). However, for the high-frequency asymptotics, only the $\mathcal{O}(1)$ terms, resulting from the potential flow theory calculations of §2.5.1, match with previous studies. Additionally, the coefficients of the $\mathcal{O}(\eta^{-1}\ln\eta)$ and $\mathcal{O}(\eta^{-1})$ terms are computed numerically and are listed in table 2 for reference.

Of particular significance is the presence of $\mathcal{O}(\eta^{-1}\ln\eta)$ terms in the high-frequency expansions. These terms were previously overlooked in the literature, yet they play a critical role in accurately capturing the behaviour of the oscillating disk in the high-frequency regime. While prior studies have hinted at a singular limit when transitioning from an oscillating oblate spheroid to a zero-thickness disk (Loewenberg 1993; Zhang & Stone 1998), our analysis rigorously confirms the necessity of incorporating logarithmic terms alongside the inverse frequency terms. To further support the inclusion of $\mathcal{O}(\eta^{-1}\ln\eta)$ terms, below, we present an asymptotic analysis of the integrals involved in (2.26).

3.2. *Evaluating integrals appearing in (2.26) in the limit of $\eta \to \infty$*

For clarity, we first establish our argument for a representative case before extending it to more general scenarios. Specifically, we consider the case where $m = 0$ and $n = 1$, in which the corresponding integral can be split into three parts as follows:

$$\int_0^\infty k\left(1 - \frac{k}{\xi}\right) J_{1/2}(k)\, J_{5/2}(k)\, \mathrm{d}k = \int_0^1 k\left(1 - \frac{k}{\xi}\right) J_{1/2}(k)\, J_{5/2}(k)\, \mathrm{d}k$$
$$+ \int_1^\eta k\left(1 - \frac{k}{\xi}\right) J_{1/2}(k)\, J_{5/2}(k)\, \mathrm{d}k$$
$$+ \int_\eta^\infty k\left(1 - \frac{k}{\xi}\right) J_{1/2}(k)\, J_{5/2}(k)\, \mathrm{d}k, \quad (3.1)$$

where the relevant Bessel functions and their product are given by

$$J_{1/2}(k) = \sqrt{\frac{2}{\pi k}} \sin k, \quad (3.2)$$

$$J_{5/2}(k) = \sqrt{\frac{2}{\pi k}} \left[\left(\frac{3}{k^2} - 1\right) \sin k - \frac{3\cos k}{k}\right], \quad (3.3)$$

$$J_{1/2}(k) J_{5/2}(k) = \frac{1}{\pi k}\left[\left(\frac{3}{k^2} - 1\right) + \left(1 - \frac{3}{k^2}\right)\cos 2k - \frac{3}{k}\sin 2k\right]. \quad (3.4)$$

The term in the parenthesis in (3.1) can be expanded as a Taylor series in the region $k \leqslant \eta$ as
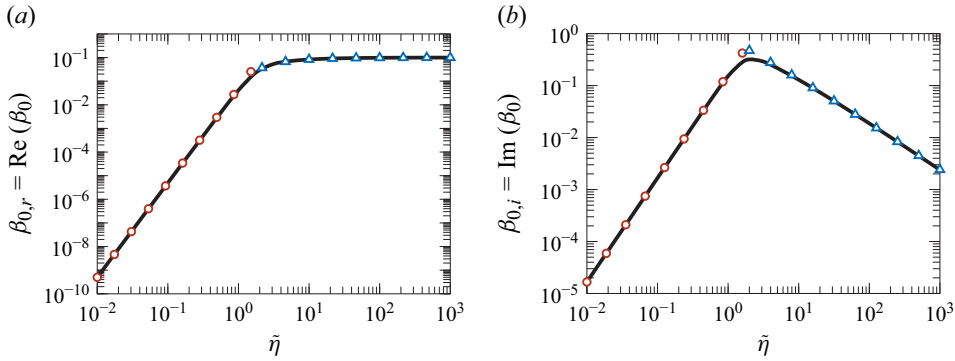
Figure 3. Plots of the (*a*) real and (*b*) imaginary components of β versus $\tilde{\eta} = \eta\varepsilon$. Red circular and blue triangular symbols correspond to the asymptotic formulas for the limits of $\tilde{\eta} \to 0$ and $\tilde{\eta} \to \infty$, respectively, as listed in table 1.

$$
1 - \frac{k}{\xi} = 1 - \frac{(k/\eta)}{\sqrt{2}} \left[1 + \frac{(k/\eta)^2}{2} \right] + \cdots + i \frac{(k/\eta)}{\sqrt{2}} \left[1 - \frac{(k/\eta)^2}{2} \right] + \cdots. \tag{3.5}
$$

Similarly, in the region $k \geqslant \eta$, it takes the form

$$
1 - \frac{k}{\xi} = \frac{3 (\eta/k)^4}{8} \left[1 - \frac{35 (\eta/k)^4}{48} \right] + \cdots + i \frac{(\eta/k)^2}{2} \left[1 - \frac{5 (\eta/k)^4}{8} \right] + \cdots. \tag{3.6}
$$

Substituting (3.4) and these expansions in the integrals on the right-hand side of (3.1), we find that a term proportional to $(k\eta)^{-1}$ emerges in the middle integral, covering the range $1 \leqslant k \leqslant \eta$. The integral of this term contributes a term proportional to $\ln \eta$, thereby justifying the appearance of $\mathcal{O}(\eta^{-1} \ln \eta)$ in the asymptotic expressions reported in table 1 for the limit $\eta \to \infty$.

This result extends naturally to other integrals, except for the special case of $m = n = 0$. In particular, the systematic emergence of an $\mathcal{O}[(k\eta)^{-1}]$ term can be demonstrated by repeating the steps outlined above and utilising the following general formula for half-integer order Bessel functions in (2.26):

$$
J_{2n+1/2}(k) = \sqrt{\frac{2}{\pi k}} \left[\mathcal{R}_{2n,1/2}(k) \sin k - \mathcal{R}_{2n-1,3/2}(k) \cos k \right]. \tag{3.7}
$$

Here, the Lommel polynomial is defined as

$$
\mathcal{R}_{\ell,\nu}(k) = \sum_{l=0}^{[\ell/2]} \frac{(-1)^l (\ell - l)! \Gamma(\ell - l + \nu)}{l! (\ell - 2l)! \Gamma(l + \nu)} \left(\frac{2}{k} \right)^{\ell - 2l}, \tag{3.8}
$$

where the square brackets denote the floor function, which rounds down to the nearest integer.

3.3. *Added mass and damping coefficients of an annular disk*

As the final step, we solve an additional linear system of equations based on (2.40) to determine β_m over the range $10^{-2} \leqslant \tilde{\eta} \leqslant 10^3$. For small values of $\tilde{\eta}$, we retain the first ten terms in the series, progressively increasing this count to a maximum of forty terms for the largest $\tilde{\eta}$ considered. The results for β_0 are presented in figure 3, where symbols denote the asymptotic expressions reported in table 1. As previously indicated, the coefficients in

this table that are not directly derived from the analyses of §§ 2.4 and 2.5 are computed numerically (see table 2). Once again, we observe the remarkable accuracy of these simple formulas in capturing the variations of both the real and imaginary components of β_0 as functions of $\tilde{\eta}$. We note that the inclusion of $\mathcal{O}(\tilde{\eta}^{-1} \ln \tilde{\eta})$ terms in the asymptotic limit of $\tilde{\eta} \to \infty$ follows from the same reasoning used in § 3.2. Naturally, for the integrals in (2.40), different Taylor series expansions must be employed for the term that is multiplied by the product of Bessel functions.

With β_0 determined, alongside the previously computed $p^\star$ and α_0 from the baseline problem, we now analyse the added mass and damping coefficients of the annular disk (see (2.5), (2.17), (2.28) and (2.41)). The solid black lines in figures 4 and 5 illustrate the variations of the normalised added mass and damping coefficients (a/a_0 and b/b_0, respectively) as functions of the pore size (ε) across a broad range of oscillatory Reynolds numbers (η). From top to bottom, the rows in figure 4 correspond to $\eta = 10^{-2}$, 10^{-1} and 10^0, while those in figure 5 represent $\eta = 10^1$, 10^2 and 10^3. The red circles, purple squares, and blue triangles denote, respectively, the asymptotic formulas listed in table 3 (derived from table 1) in the limits of $\eta \to 0$, $\eta \to \infty$ and $\tilde{\eta} \to 0$ and $\eta \to \infty$ and $\tilde{\eta} \to \infty$. Insets highlight deviations of the normalised coefficients from unity, emphasising how porosity-induced corrections to the added mass and damping coefficients scale with ε in different regimes (see table 3).

The green dashed curves in figures 4 and 5 represent the results of a numerical solution to the original problem (i.e. (2.3) and (2.4)) in the frequency domain, obtained using a second-order finite-element approach as implemented in COMSOL Multiphysics (Zimmerman 2006; Pepper & Heinrich 2017). These results serve as a benchmark for assessing the accuracy of our small-pore assumption, which led us to retain only the leading term in the Taylor series expansion of $\hat{p}_0$ in (2.29). To model the unbounded domain in the simulations, the outer boundary was approximated as a large hemisphere centred at the disk's midpoint. The radius of this hemisphere was varied between $100R$ and $2000R$ depending on the value of η. The two-dimensional axisymmetric computational domain was discretised using triangular elements with adaptive mesh refinement to ensure accuracy and efficiency. The validity of this numerical approach was confirmed through comparison with the calculations in § 3.1 for a solid disk, as well as through grid and domain-size independence studies, which verified that the computed added mass and damping coefficients changed by less than 1 % upon further refinement.

A preliminary examination of both figures reveals that our asymptotic formulas accurately capture the behaviour of normalised coefficients over a broad range of ε, demonstrating remarkable precision except for the high-η asymptote's subpar performance in figure 5(b). Furthermore, our theoretical predictions closely align with finite-element simulations for ε up to 1/2, and in many cases, even beyond.

A closer inspection indicates that both normalised coefficients trend downward with increasing pore size for $\eta \lesssim 1$. As highlighted in the insets, their departures from unity follow a ε^3 scaling (see figure 4). For $\eta \lesssim 10^{-1}$, the asymptotic expressions for $\eta \to 0$ provide excellent accuracy but become less reliable as η grows. At larger η, the behaviour of a/a_0 is well described by a combination of asymptotic formulas for $\eta \to 0$ and $\tilde{\eta} \to 0$ at small pore sizes, and $\eta \to \infty$ and $\tilde{\eta} \to \infty$ at bigger pore sizes. In this regime, the initial ε^3 scaling for the decrease in a/a_0 transitions to a linear trend as ε increases (see the left column of figure 5).

A key finding of this study is that, for $\eta \gtrsim 1$, while the added mass coefficient continues to decrease with increasing the pore size, the damping coefficient initially rises with ε, reaches a peak and then declines as the pore size increases further. This initial increase is predicted by our asymptotic analysis, which anticipates a rise proportional to ε^3
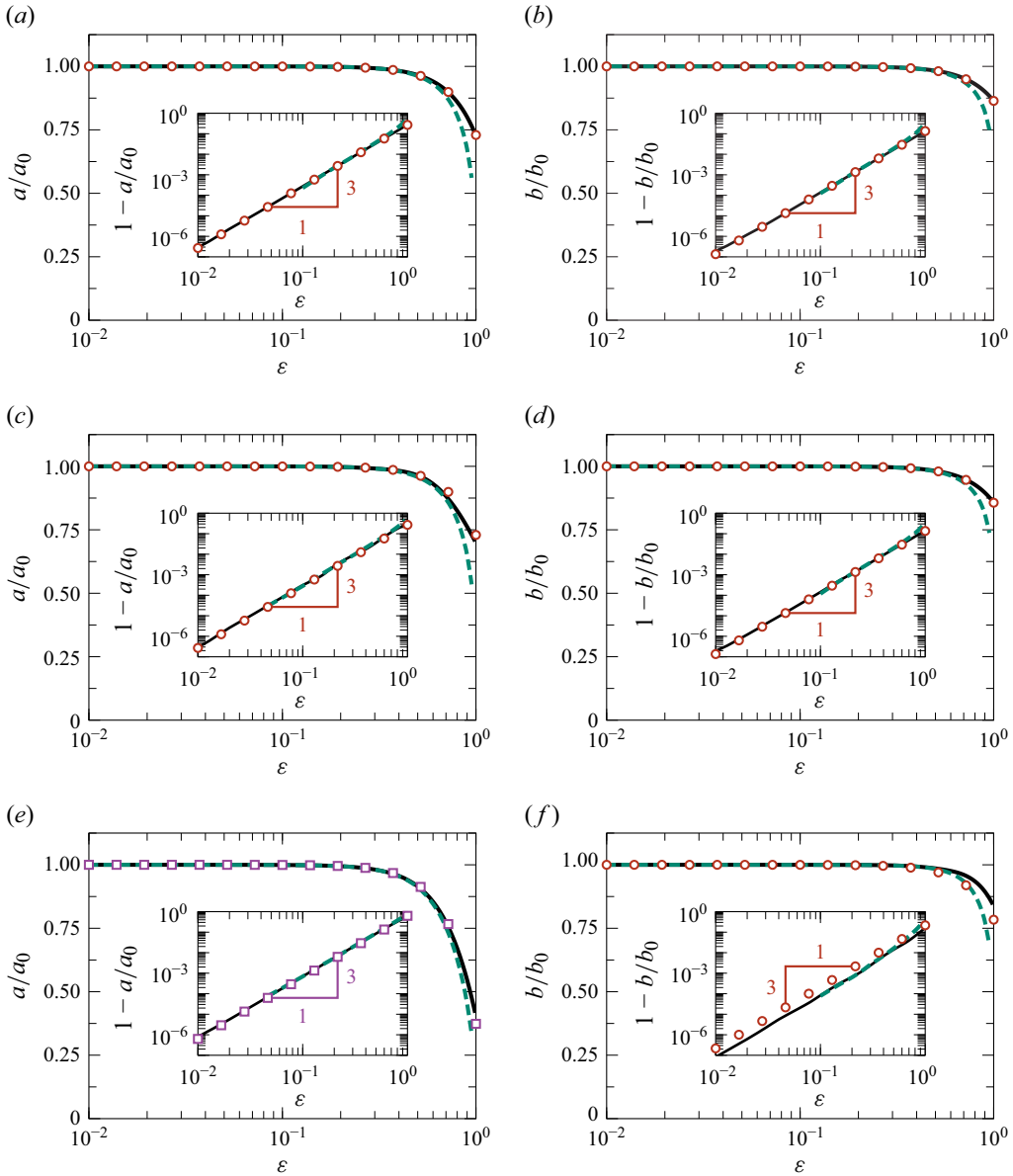
Figure 4. Plots of a/a_0 (left column) and b/b_0 (right column) versus ε. The top, middle and bottom rows correspond to $\eta = 10^{-2}$, 10^{-1} and 10^0, respectively. The solid black lines represent our theoretical calculations, whereas the dashed green curves show the results from finite-element numerical simulations. The inset plots illustrate the deviations of the normalised coefficients from unity. The red circles and purple squares denote the asymptotic formulas from table 3 in the limiting cases of $\eta \to 0$, and $\eta \to \infty$ and $\tilde{\eta} \to 0$, respectively.

(see § 2.5.2 and table 3). Notably, despite the oscillatory Reynolds number based on the disk's outer radius (η) being high, the Reynolds number based on the pore radius, $\tilde{\eta} = \eta\varepsilon$, remains well below unity. The contrast in regimes between the first and second problems gives rise to the initial enhancement of the damping coefficient due to porosity.

The peak of b/b_0 and its corresponding pore size (ε_{max}) are nicely predicted by our asymptotic formula in the limit of $\eta \to \infty$ and $\tilde{\eta} \to \infty$ for $\eta \gtrsim 10^2$ (see the last two rows
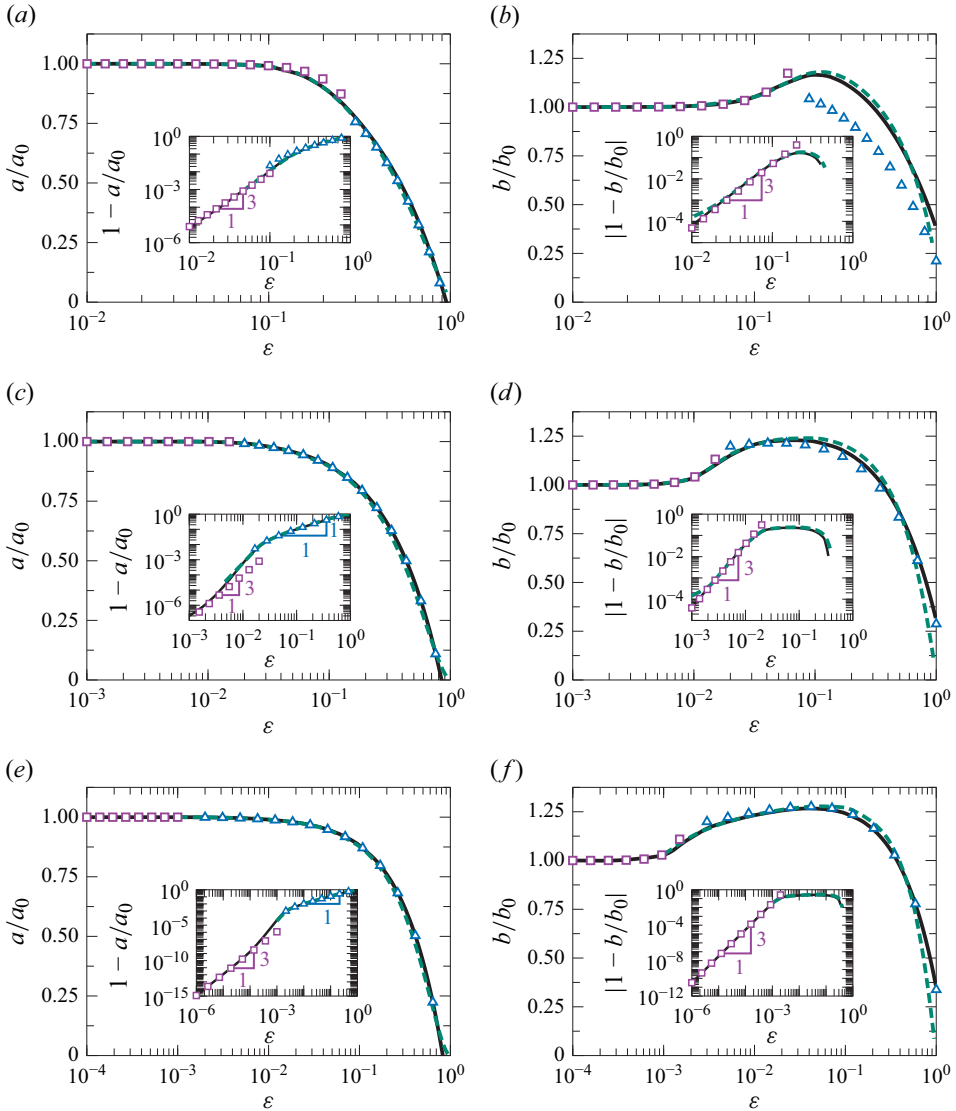
Figure 5. Plots of a/a_0 (left column) and b/b_0 (right column) versus ε. The top, middle and bottom rows correspond to $\eta = 10^1$, 10^2 and 10^3, respectively. The solid black lines represent our theoretical calculations, whereas the dashed green curves show the results from finite-element numerical simulations. The inset plots illustrate the deviations of the normalised coefficients from unity. The purple squares and blue triangles denote the asymptotic formulas from table 3 in the limiting cases of $\eta \to \infty$ and $\tilde{\eta} \to 0$, and $\eta \to \infty$ and $\tilde{\eta} \to \infty$, respectively.

of the right column of figure 5). By setting the derivative of the asymptotic formula for b/b_0 with respect to ε to zero, we obtain

$$\varepsilon_{max} = \frac{\mathcal{A}_i^\beta}{\pi \left(\mathcal{A}_r^p \ln \eta + \mathcal{B}_r^p \right)}. \tag{3.9}$$

Figure 6 illustrates the variations of ε_{max} and the corresponding b/b_0 and a/a_0 as functions of η, with asymptotic predictions denoted by blue triangles. As evident from (3.9), ε_{max} decreases logarithmically with increasing η. In the asymptotic limit $\eta \to \infty$,

1017 A21-16

Asymptotic limits	a/a_0
$\eta \to 0$	$1 - \dfrac{8\varepsilon^3}{3\pi^2}$
$\eta \to \infty, \ \tilde{\eta} \to 0$	$1 - \dfrac{2\eta}{\pi}\left(\mathcal{A}_r^p \ln \eta + \mathcal{B}_r^p\right)\varepsilon^3$
$\eta \to \infty, \ \tilde{\eta} \to \infty$	$1 - \dfrac{96}{\pi^2}\dfrac{\varepsilon\left[\eta + \pi\left(\mathcal{A}_i^p \ln \eta + \mathcal{B}_i^p\right)\right] - \left[\mathcal{A}_r^\beta \ln(\varepsilon\eta) + \mathcal{B}_r^\beta\right]}{8\eta + 3(\mathcal{A}_a \ln \eta + \mathcal{B}_a)}$

	b/b_0
$\eta \to 0$	$1 - \dfrac{4\varepsilon^3}{3\pi^2}\left(1 + \dfrac{4\sqrt{2}}{3\pi}\eta\right)$
$\eta \to \infty, \ \tilde{\eta} \to 0$	$1 + \dfrac{16(\varepsilon\eta)^3}{3\pi^2(\mathcal{A}_b \ln \eta + \mathcal{B}_b)}$
$\eta \to \infty, \ \tilde{\eta} \to \infty$	$1 + \dfrac{32\left\{\left[\mathcal{A}_i^\beta \ln(\varepsilon\eta) + \mathcal{B}_i^\beta\right] - \pi\varepsilon\left(\mathcal{A}_r^p \ln \eta + \mathcal{B}_r^p\right)\right\}}{\pi^2(\mathcal{A}_b \ln \eta + \mathcal{B}_b)}$

Table 3. Asymptotic expressions for the normalised added mass and damping coefficients (a/a_0 and b/b_0, respectively) in the limiting cases of $\eta \to 0$, $\eta \to \infty$ and $\tilde{\eta} \to 0$ and $\eta \to \infty$ and $\tilde{\eta} \to \infty$. These formulas are derived based on those reported in table 1. The value of the coefficients $\mathcal{A}$ and $\mathcal{B}$ are given in table 2.
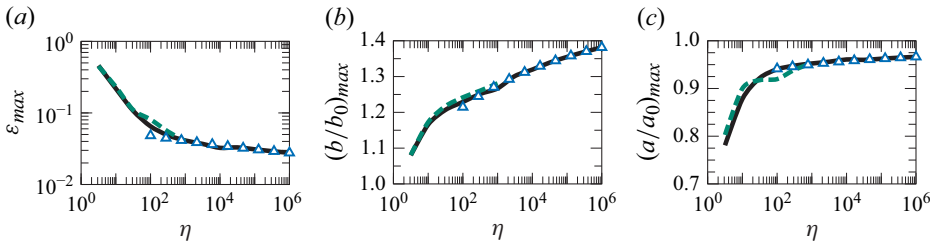

Figure 6. Plots of (*a*) the pore size corresponding to the maximum normalised damping coefficient (ε_{max}), (*b*) the peak value of b/b_0, and (*c*) a/a_0 at ε_{max}, all as functions of η. The solid black lines represent our theoretical calculations, whereas the dashed green curves show the results from finite-element numerical simulations. Also, the blue triangles represent the predictions from (3.9) and its substitution into the asymptotic formulas for b/b_0 and a/a_0 in the limit $\eta \to \infty$ and $\tilde{\eta} \to \infty$, as reported in table 3.

b/b_0 and a/a_0 approach very slowly to 1.62 and 1, respectively. Although achieving about 60 % damping improvement may be challenging due to the requirement of very high η, reaching a 30 % enhancement is feasible in many engineering applications.

To conclude this section, we analyse the supplementary plots in figure 7, which depict the variations of the following two quantities with ε for the considered values of η:

$$\frac{|F|}{|F_0|} = \frac{\sqrt{a^2 + b^2}}{\sqrt{a_0^2 + b_0^2}}, \tag{3.10}$$
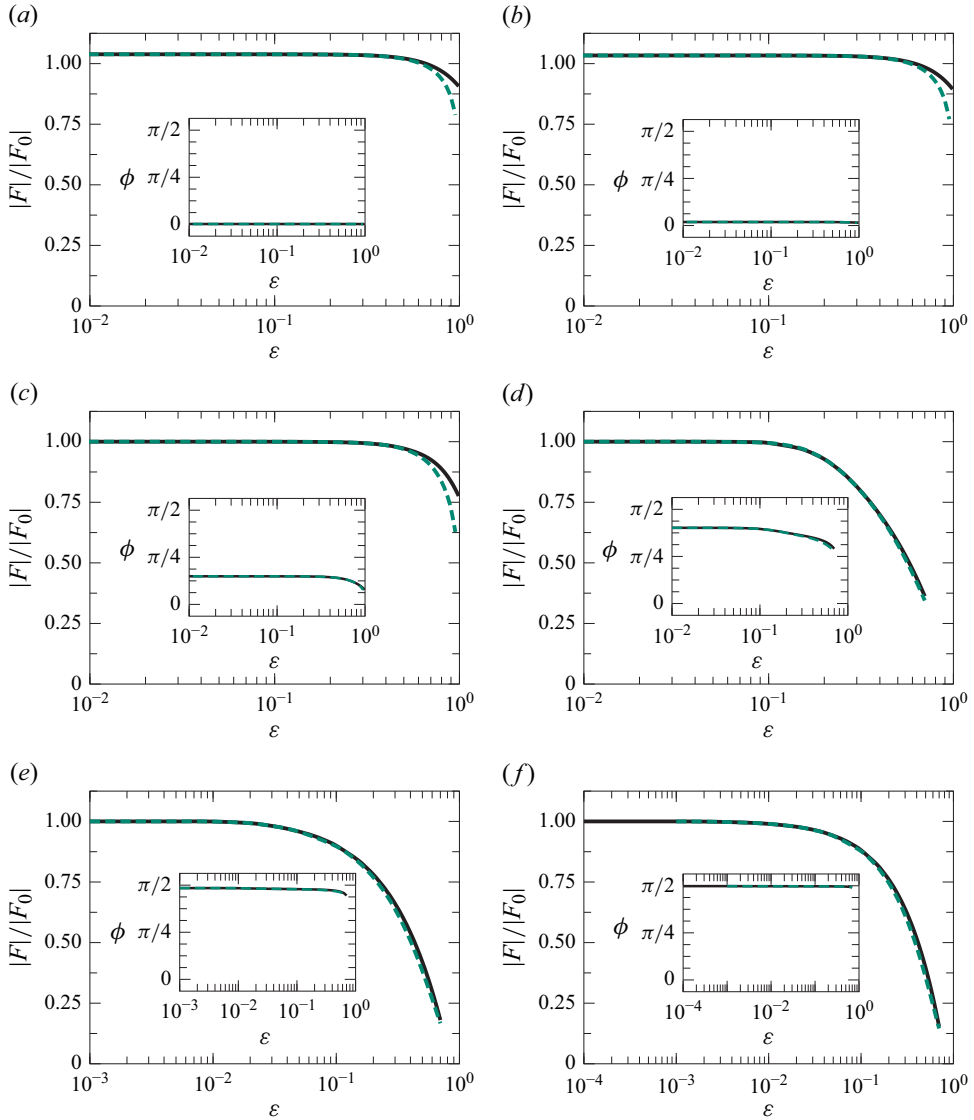
$$\phi = \tan^{-1}\left(\frac{a}{b}\right). \tag{3.11}$$

Figure 7. (*a*)–(*f*) plots of the normalised total force $|F|/|F_0|$ versus ε for η, with the insets showing the corresponding variations of the phase angle ϕ as a function of ε. The panels correspond to $\eta = 10^{-2}$ (*a*), 10^{-1} (*b*), 1 (*c*), 10 (*d*), 10^2 (*e*) and 10^3 (*f*). Also, the green dashed lines represent the results of finite-element numerical simulations.

As before, dashed green lines indicate simulation results. A notable observation is that, despite the increase in the damping coefficient for sufficiently high η, the normalised total force always trends downward due to porosity, regardless of the oscillatory Reynolds number (see the main panels of figure 7). Furthermore, the phase angle ϕ increases from 0 to $\pi/2$ as η approaches ∞ (see the insets of figure 7). To reconcile the contrasting behaviours of the normalised total force with that of the normalised damping coefficient, we consider the relation

$$b = \frac{|F|}{\eta^2} \cos \phi. \tag{3.12}$$

At sufficiently high η, the reduction in the total force due to the porosity of the disk is more than offset by the decrease in the phase angle. Since ϕ approaches $\pi/2$ in this regime, even a small decrease in ϕ leads to a relatively large change in the magnitude of $\cos\phi$, thereby influencing the damping behaviour significantly. This counterintuitive increase in the damping coefficient is thus purely a result of the phase shift effect and not due to additional flow separation or vortex shedding.

4. Summary

We developed a semi-analytical framework to investigate the hydrodynamics of an annular disk undergoing small-amplitude, broadside sinusoidal oscillations in an unbounded fluid. Utilising the superposition principle, the reciprocal theorem and asymptotic analysis, we systematically explored the influence of porosity and oscillation frequency on the disk's added mass and damping coefficients. By decomposing the problem into two sub-problems – one describing a solid disk in heave motion and the other modelling flow through a circular orifice in an infinite wall – we derived asymptotic expressions that accurately capture the variations of the hydrodynamic coefficients across a wide range of oscillatory Reynolds numbers and pore sizes. Numerical simulations confirmed the validity of our asymptotic formulations, demonstrating their accuracy for inner-to-outer radius ratios up to at least $1/2$.

A key finding of our analysis is the identification of a previously overlooked logarithmic term in the high-frequency asymptotic expansions, which plays a crucial role in accurately characterising the behaviour of the added mass and damping coefficients. More importantly, we uncovered a non-trivial dependence of the damping coefficient on pore size. While the added mass coefficient decreases monotonically with increasing porosity, the damping coefficient initially rises, reaching a maximum before eventually declining. Remarkably, in the extreme inertial limit, the peak damping coefficient surpasses that of a solid disk by up to $62\,\%$, potentially challenging conventional assumptions about how porosity affects oscillatory fluid–structure interactions. The transition from a viscosity-dominated regime to an inertial regime reveals intricate interplay between permeability effects and oscillatory flow behaviour, highlighting the complex role of porosity in the fluid–structure dynamics.

These insights have considerable implications for engineering applications such as designing offshore platforms and wave energy converters, where porosity could be strategically optimised to enhance stability and efficiency. Our findings suggest that tuning porosity offers a promising means of controlling hydrodynamic forces, particularly in high-frequency oscillatory environments. Future work may extend this framework to explore nonlinear effects or larger pore geometries; while this would require retaining higher-order terms and modifying parts of the derivation, leading-order nonlinear corrections may be accessible via the reciprocal theorem, and the large-pore limit could be studied by modelling the annular disk as a ring, following Davis (1991*b*).

Declaration of interests. The authors declare no conflict of interest.

REFERENCES

AN, S. & FALTINSEN, O.M. 2013 An experimental and numerical study of heave added mass and damping of horizontally submerged and perforated rectangular plates. *J. Fluids Struct.* **39**, 87–101.

AURELI, M., BASARAN, M.E. & PORFIRI, M. 2012 Nonlinear finite amplitude vibrations of sharp-edged beams in viscous fluids. *J. Sound Vib.* **331** (7), 1624–1654.

BROWN, A.C. & THOMSON, J. 2015 Heave plate dynamics for a point absorbing wave energy converter. In *3rd Annual Marine Energy Technology Symposium (METS)*, pp. 5.

CHUA, K.H., CLELLAND, D., HUANG, S. & SWORN, A. 2005 Model experiments of hydrodynamic forces on heave plates. In *International Conference on Offshore Mechanics and Arctic Engineering*, vol. 41952, pp. 943–948.

DAVIS, A.M.J. 1991*a* Shear flow disturbance due to a hole in the plane. *Phys. Fluids* **3** (3), 478–480.

DAVIS, A.M.J. 1991*b* Slow viscous flow due to motion of an annular disk; pressure-driven extrusion through an annular hole in a wall. *J. Fluid Mech.* **231**, 51–71.

DOWNIE, M.J., GRAHAM, J.M.R., HALL, C., INCECIK, A. & NYGAARD, I. 2000*a* An experimental investigation of motion control devices for truss spars. *Mar. Struct.* **13** (2), 75–90.

DOWNIE, M.J., WANG, J. & GRAHAM, J.M.R. 2000*b* The effectiveness of porous damping devices. In *ISOPE International Ocean and Polar Engineering Conference*, pp. ISOPE-I-00-275.

ERDOGAN, F. & BAHAR, L.Y. 1964 On the solution of simultaneous dual integral equations. *SIAM J. Appl. Maths* **12** (3), 666–675.

EZOJI, M., SHABAKHTY, N. & TAO, L. 2022 Hydrodynamic damping of solid and perforated heave plates oscillating at low KC number based on experimental data: a review. *Ocean Eng.* **253**, 111247.

GRADSHTEYN, I.S. & RYZHIK, I.M. 2007 *Table of Integrals, Series, and Products*. Academic press.

HAPPEL, J. & BRENNER, H. 1983 *Low Reynolds Number Hydrodynamics, with Special Applications to Particulate Media*. Martinus Nijhoff.

HE, H. 2003 *Hydrodynamics of Thin Plates*. University of Michigan.

JAFARI KANG, S., DEHDASHTI, E., VANDADI, V. & MASOUD, H. 2019 Optimal viscous damping of vibrating porous cylinders. *J. Fluid Mech.* **874**, 339–358.

LAMB, H. 1945 *Hydrodynamics*. Dover Publications.

LI, J., LIU, S., ZHAO, M. & TENG, B. 2013 Experimental investigation of the hydrodynamic characteristics of heave plates using forced oscillation, **66**, 82–91.

LIU, Y., LI, H., LI, Y. & HE, S. 2011 A new approximate analytic solution for water wave scattering by a submerged horizontal porous disk. *Appl. Ocean Res.* **33** (4), 286–296.

LOEWENBERG, M. 1993 The unsteady stokes resistance of arbitrarily oriented, finite-length cylinders. *Phys. Fluids* **5** (11), 3004–3006.

MASOUD, H. & STONE, H.A. 2019 The reciprocal theorem in fluid dynamics and transport phenomena. *J. Fluid Mech.* **879**, P1.

MENTZONI, F. & KRISTIANSEN, T. 2019*a* Numerical modeling of perforated plates in oscillating flow. *Appl. Ocean Res.* **84**, 1–11.

MENTZONI, F. & KRISTIANSEN, T. 2019*b* A semi-analytical method for calculating the hydrodynamic force on perforated plates in oscillating flow. In *International Conference on Offshore Mechanics and Arctic Engineering*, vol. 58844, pp. V07AT06A015. American Society of Mechanical Engineers.

MENTZONI, F. & KRISTIANSEN, T. 2020 Two-dimensional experimental and numerical investigations of perforated plates in oscillating flow, orbital flow and incident waves. *Appl. Ocean Res.* **97**, 102078.

MOLIN, B. 1993 A potential flow model for the drag of shrouded cylinders. *J. Fluids Struct.* **7** (1), 29–38.

MOLIN, B. 2001 On the added mass and damping of periodic arrays of fully or partially porous disks. *J. Fluids Struct.* **15** (2), 275–290.

MOLIN, B. 2011 Hydrodynamic modeling of perforated structures. *Appl. Ocean Res.* **33** (1), 1–11.

MOLIN, B., REMY, F. & RIPPOL, T. 2007 Experimental study of the heave added mass and damping of solid and perforated disks close to the free surface. In *Proceedings of the 12th International Maritime Association of the Mediterranean (IMAM) 2007*.

NOKOB, M.H. & YEUNG, R.W. 2018 Added mass of thin flat plates of arbitrary shapes with possible openings. *Appl. Ocean Res.* **79**, 149–159.

PEPPER, D.W. & HEINRICH, J.C. 2017 *The Finite Element Method: Basic Concepts and Applications with MATLAB, MAPLE, and COMSOL*. CRC Press.

SHERWOOD, J.D. 2020 Unsteady flow adjacent to an oscillating or impulsively started porous wall. *J. Fluid Mech.* **894**, A1.

SNEDDON, I.N. 1966 *Mixed Boundary Value Problems in Potential Theory*. North-Holland Publishing Company.

TAMAKUWALA, R., USMAN, M., TOM, N.M. & MASOUD, H. 2025 Performance of a two-body wave energy converter. *Flow*. (Under review).

TANZOSH, J.P. & STONE, H.A. 1996 A general approach for analyzing the arbitrary motion of a circular disk in a Stokes flow. *Chem. Engng Commun.* **148** (1), 333–346.

TAO, L. & DRAY, D. 2008 Hydrodynamic performance of solid and porous heave plates **35** (10), 1006–1014.

TRANTER, C. 1966 *Integral Transforms in Mathematical Physics*. Methuen & Co.

VU, K.H., CHENU, B. & THIAGARAJAN, K.P. 2004 Hydrodynamic damping due to porous plates. In *Proceedings of the World Scientific and Engineering Academy and Society. WSEAS, Corfu, Greece*, pp. 17–19.

WADHWA, H. 2011 Hydrodynamics of porous plates and influence of free surface proximity. PhD thesis, University of Western Australia, Australia.

WADHWA, H., THIAGARAJAN, K. & PISTANI, F. 2009 Experimental visualization of flows induced by solid and porous oscillating disks. In *Proceedings of 8th International Symposium on Particle Image Velocimetry (PIV 09), Melbourne, Victoria, Australia, August 25-28*.

WILLIAMS, W.E. 1966 A note on slow vibrations in a viscous fluid. *J. Fluid Mech.* **25** (3), 589–590.

ZHANG, W. & STONE, H.A. 1998 Oscillatory motions of circular disks and nearly spherical particles in viscous flows. *J. Fluid Mech.* **367**, 329–358.

ZIMMERMAN, W.B.J. 2006 *Multiphysics Modeling with Finite Element Methods*. World Scientific Publishing Company.